Journal of Alloys and Compounds 1084 (2026) 191984

Contents lists available at ScienceDirect

Journal of Alloys and Compounds

journal homepage: www.elsevier.com/locate/jalcom

MOF-derived $NiCo_2O_4$/NiO mixed oxide-carbon nanofiber composite for sensitive electrochemical detection of vanillin

P. Varatharajan [a,1], Kumar Gokulkumar [a,1], Neeraja Bose [a], Shih-Hsuan Chen [a], Kun-Mu Lee [a,b,c,d,*]

[a] Center for Sustainability and Energy Technologies, Chang Gung University, Taoyuan, 33302, Taiwan
[b] Department of Chemical and Materials Engineering, Chang Gung University, Taoyuan, 33302, Taiwan
[c] Division of Neonatology, Department of Pediatrics, Chang Gung Memorial Hospital, Linkou, Taoyuan, 33305, Taiwan
[d] College of Environment and Resources, Ming Chi University of Technology, New Taipei City, 24301, Taiwan

ARTICLE INFO

Keywords:
Mixed-metal oxide
Metal oxide-carbon composite
Interfacial charge transfer
Screen-printed carbon electrode
Vanillin detection

ABSTRACT

The food industry widely uses vanillin (VLN) as a flavouring compound, creating a need for reliable analytical methods for its routine determination in food products. In this work, a MOF-derived mixed metal oxide integrated with carbon nanofibers ($NiCo_2O_4$/NiO@CNF) was developed for the electrochemical determination of VLN. A bimetallic NiCo-MOF precursor was first prepared by a solvothermal method and subsequently converted by calcination into a crystalline $NiCo_2O_4$/NiO, followed by integration with conductive CNF through ultrasonication. Structural, surface, and morphological characterization confirmed the formation of the mixed metal oxide and its association with CNF. The resulting $NiCo_2O_4$/NiO@CNF modified screen printed carbon electrode (SPCE) showed improved charge transfer characteristics and a pronounced electrocatalytic response toward VLN oxidation. Electrochemical analysis indicated a mixed diffusion/surface controlled, irreversible proton-coupled electron transfer process. The sensor exhibited two linear concentration ranges of 0.10–6.50 and 8.23–86 μmol L^{-1}, with a sensitivity of 2.07 μA μmol^{-1} cm^{-2} and a detection limit (LOD) of 6.65 nmol L^{-1}. The electrode showed good selectivity, reproducibility (RSD = 3.34%) and storage stability (RSD = 4.42%). The method was successfully applied to real food samples including ice cream, cookies, and chocolate, achieving recoveries ranging from 95% to 100% and RSD values below 2.5%, demonstrating the applicability of the method to VLN determination in food samples.

1. Introduction

Flavouring substances play an important role in the formulation of processed foods because they contribute to aroma and taste and help maintain desirable sensory characteristics. Among the numerous flavouring agents used commercially, vanillin (VLN), chemically identified as 4-hydroxy-3-methoxybenzaldehyde, is widely employed in the food and beverage, household cleaning, cosmetic and pharmaceutical industries [1–3]. It is naturally obtained from the pods of Vanilla planifolia and possesses a characteristic aromatic structure containing hydroxyl, methoxy, and aldehyde functional groups [4]. The characteristic taste and fragrance of VLN have led to its extensive use in products such as chocolate, ice cream, biscuits, beverages, baked foods, edible oils, and pharmaceutical preparations [5–7]. Besides its flavouring properties, VLN has demonstrated diverse biological activities, including antioxidant, antimicrobial, anti-inflammatory and neuroprotective effects in experimental studies[6,8,9]. However, excessive intake or uncontrolled addition of VLN may lead to deleterious effects, including headache, nausea, cytotoxicity, liver and kidney dysfunction, and organ enlargement following prolonged exposure [10,11]. Therefore, the Joint FAO/WHO Expert Committee on Food Additives (JECFA) established an acceptable daily intake (ADI) for VLN of 0–10 mg kg^{-1} body weight per day. Consequently, monitoring VLN concentrations in food products is important for assessing dietary exposure and ensuring that its intake remains within acceptable levels [12,13].Given the extensive use of VLN in food products and the possible adverse effects of excessive intake, reliable analytical approaches with high sensitivity, selectivity, and rapid response are needed for precise VLN determination and effective

* Corresponding author at: Center for Sustainability and Energy Technologies, Chang Gung University, Taoyuan 33302, Taiwan.
E-mail address: kmlee@mail.cgu.edu.tw (K.-M. Lee).
[1] The authors contributed equally to this work.

https://doi.org/10.1016/j.jallcom.2026.191984
Received 18 August 2026; Received in revised form 22 October 2026; Accepted 25 October 2026
Available online 26 October 2026
0925-8388/© 2026 Elsevier B.V. All rights are reserved, including those for text and data mining, AI training, and similar technologies.

food-safety assessment.

Electrochemical sensing methods have attracted considerable interest for VLN determination because of their fast response, simple operation, excellent sensitivity, and suitability for real-time food analysis [14–16]. The electrochemical activity of modified electrodes can be substantially improved through the integration of functional nanomaterials, which provide a high specific surface area, numerous catalytic sites, and efficient electron-transfer pathways, thereby facilitating the reliable determination of VLN at very low concentrations [17]. Conventional methods offer reliable VLN quantification but often involve complex instrumentation, costly analysis, and time-consuming sample preparation. In contrast, electrochemical sensing enables rapid, sensitive, and economical VLN detection with simpler operation [18–20].

Metal–organic frameworks have attracted considerable interest as transient templates for the fabrication of porous transition-metal oxides because they provide uniformly distributed metal centers, controllable morphology, and well-organized coordination architectures [21]. In Ni-Co-based MOFs, the metal ions are periodically interconnected through organic terephthalate ligands, forming highly ordered frameworks with homogeneous elemental distribution at the molecular level [22,23]. Such structural uniformity is difficult to achieve using conventional oxide synthesis methods, including co-precipitation, solid--state reactions, or direct hydrothermal synthesis, where rapid nucleation and uncontrolled particle growth frequently lead to severe agglomeration, irregular morphology, non-uniform elemental dispersion, and reduced exposure of catalytically active sites [24,25]. In contrast, MOF-derived synthesis enables precise structural evolution during thermal conversion, allowing the precursor morphology to be retained while generating highly porous and defect-containing oxide architectures [26,27].

During calcination, the coordinated organic ligands within the MOF framework undergo thermal decomposition and are gradually removed in the form of gaseous carbonaceous species [25]. This process converts the insulating metal-organic coordination structure into crystalline mixed-metal oxides while simultaneously generating internal pores, structural vacancies, and exposed active surfaces throughout the material [24]. The elimination of the organic framework is particularly important because the organic ligands in pristine MOFs generally possess poor electrical conductivity and can hinder efficient electron migration during electrochemical reactions. Therefore, thermal conversion not only enhances structural stability but also improves electrical conductivity and facilitates direct contact between the electrolyte and catalytically active metal centers. Furthermore, the gradual decomposition of the MOF skeleton can suppress excessive particle growth during crystallization, resulting in smaller crystallite domains and rough surface features with increased electrochemically accessible regions [28].

Structurally, the $NiCo_2O_4$ spinel oxide inherits the porous architecture while developing mixed-valence redox centers associated with Ni^{2+}/Ni^{3+} and Co^{2+}/Co^{3+} species [29]. The inverse spinel arrangement of $NiCo_2O_4$ promotes electron movement through the interconnected Ni-O-Co lattice, while the coexistence of NiO introduces interfacial lattice distortion and oxygen-defect regions that can accelerate charge-transfer processes [30]. Compared with directly synthesized bulk oxides, MOF-derived spinel structures generally exhibit higher porosity, improved surface roughness, better crystallographic dispersion, and increased active-site exposure due to the controlled decomposition pathway of the parent framework [24]. However, despite these advantages, spinel oxides still suffer from moderate conductivity limitations and partial structural aggregation during prolonged electrochemical operation. To further improve electron-transfer characteristics, conductive carbon nanofibers (CNFs) were incorporated as supporting materials because of their graphitic carbon structure, high electrical conductivity, and fibrous morphology [31]. The elongated conductive pathways of CNFs can facilitate rapid electron migration between oxide particles and the electrode surface while also minimizing interparticle resistance [32]. In addition, the fibrous carbon structure can effectively combine the oxide nanostructures and suppress aggregation after calcination, leading to improved structural stability and greater exposure of electrochemically active regions. Consequently, the integration of MOF-derived $NiCo_2O_4$/NiO mixed oxides with conductive CNFs $NiCo_2O_4$/NiO@CNF is expected to provide enhanced catalytic activity, faster charge-transfer kinetics, improved electrochemical durability, and superior sensing performance.

Herein, a MOF derived $NiCo_2O_4$/NiO combined with CNF was constructed for sensitive electrochemical detection of VLN in food matrices. The MOF assisted calcination strategy enabled the formation of defect containing mixed oxide structures with improved surface exposure, rich redox active sites and enhanced electrochemical activity, while the incorporation of conductive CNFs facilitated rapid electron transport and improved structural stability. The integration of mixed oxides with a conductive carbon matrix improved the electrochemical response, resulting in sensitive VLN detection over a permissible concentration range with a LOD and excellent sensitivity. Furthermore, the developed sensor demonstrated satisfactory analytical performance in real food samples including more than 95% recovery which confirming its practical applicability for food quality monitoring and safety analysis. This work expands the scope of MOF-derived mixed metal oxides-carbon composites for sensitive electrochemical detection in food-safety applications.

2. Materials and methodology

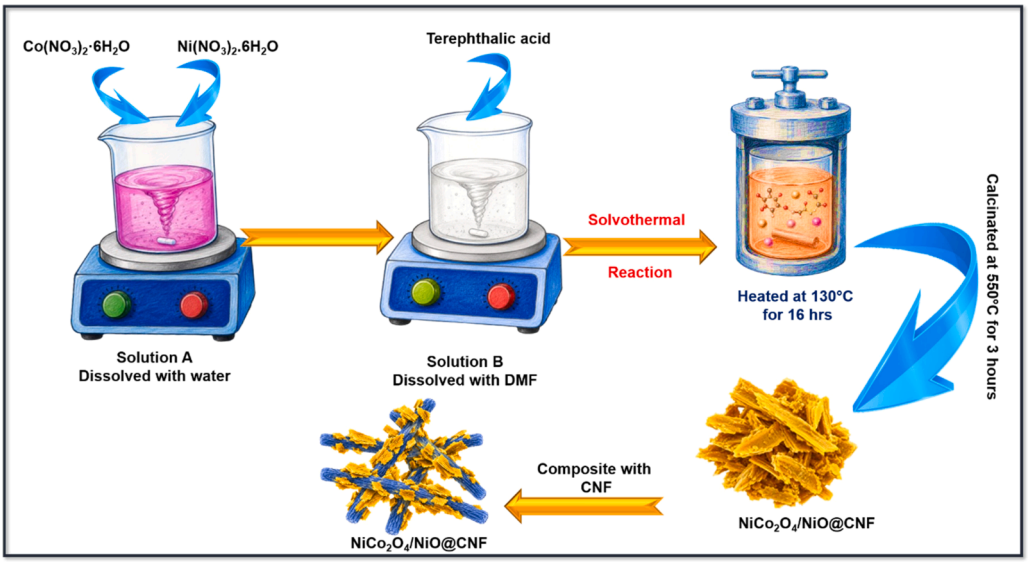
The chemicals and reagents used in this study, including their purity, suppliers, and preparation details, are provided in Section S1 of the Supporting Information. The electrochemical measurement conditions, including the electrode configuration, supporting electrolytes, and instrumental parameters employed for cyclic voltammetry (CV), differential pulse voltammetry (DPV), and electrochemical impedance spectroscopy (EIS), are described in Section S2. These supplementary sections provide additional methodological information.

2.1. Preparation of MOF-derived $NiCo_2O_4$/ NiO

Initially, 300 mg each of nickel and cobalt nitrate metal salts were dissolved in 20 mL of Millipore water to form a clear metal precursor solution (solution A). In a separate container, 600 mg of terephthalic acid (H_2BDC) was dissolved in 20 mL DMF (solution B). Under continuous stirring, solution B was introduced dropwise into solution A. After several minutes, the mixed solution gradually transformed into a pink turbid suspension, indicating the formation of the Ni-Co terephthalate coordination precursor. The mixture was continuously stirred for 1 h before being transferred to a 70 mL Teflon lined stainless steel autoclave and maintained at 130 °C for 16 h. After the reaction, the resulting Ni-Co MOF was collected and then calcinated at 550 °C for 3 h under ambient atmospheric conditions. During thermal treatment, the organic ligands were decomposed and removed, leading to the formation of crystalline MOF derived $NiCo_2O_4$/NiO mixed oxides [33].

2.2. Preparation of $NiCo_2O_4$/NiO@CNF composite

For the fabrication of the $NiCo_2O_4$/NiO@CNF composite, predetermined amounts of $NiCo_2O_4$/NiO and CNF were dispersed in ethanol at various mass ratios (1:1, 1:2 and 2:1). The mixture was subjected to ultrasonication for 40 min at room temperature to reduce particle agglomeration and promote intimate contact between the oxide particles and the CNF surface. The resulting suspension was subsequently collected and dried to obtain the $NiCo_2O_4$/NiO@CNF composite Scheme 1.



Scheme 1. Schematic representation of the preparation route for the MOF-derived $NiCo_2O_4$/NiO@CNF composite.

2.3. Preparation of Electrode Ink and SPCE Modification

For electrode fabrication, 2 mg of the synthesized $NiCo_2O_4$/NiO@CNF composite was dispersed in 1 mL of deionized water and ultrasonicated using an ultrasonic bath at a rated power of 200 W for 30 min to obtain a uniformly dispersed catalyst suspension. Subsequently, an appropriate volume of the resulting suspension was drop-cast onto the working electrode surface of the SPCE and dried in a hot-air oven at 60°C for 5 min to obtain the $NiCo_2O_4$/NiO@CNF modified SPCE. $NiCo_2O_4$/NiO, CNF and other mass ratios of $NiCo_2O_4$/NiO@CNF modified SPCE were prepared by a similar method.

3. Results and discussion

3.1. Structural, Raman and chemical state analysis

The thermal decomposition characteristics of NiCo-MOF were analysed by TGA Fig. S1. Major decomposition of the organic framework and other organic residues occurred up to approximately 470°C, followed by a stable inorganic residual mass above 500°C. Therefore, 550°C was selected as the calcination temperature to ensure complete decomposition of the organic residues and conversion of the precursor into metal oxides. The resulting crystalline phases were further characterized by XRD, Raman spectroscopy and XPS. The structural

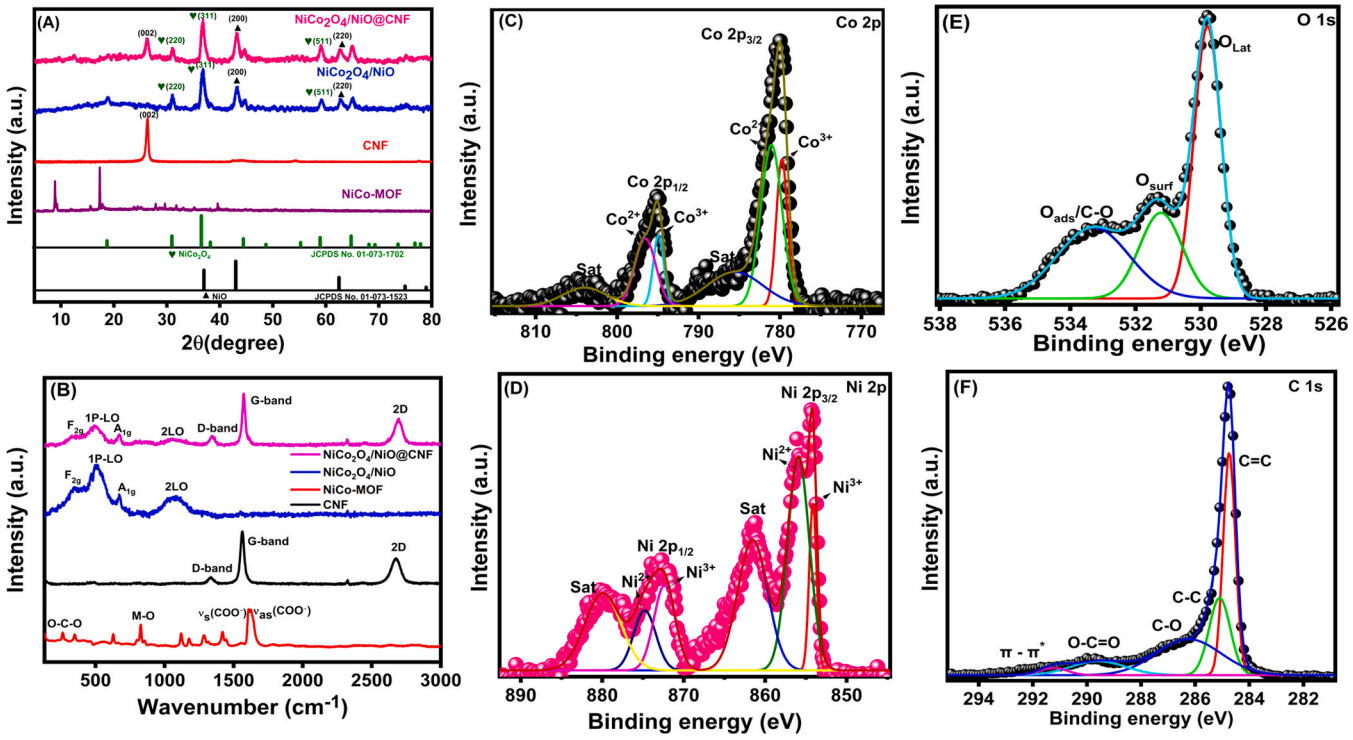


Fig. 1. (A) X-ray diffraction patterns and (B) Raman spectra of NiCo-MOF, CNF, $NiCo_2O_4$/NiO, and $NiCo_2O_4$/NiO@CNF. High-resolution deconvoluted XPS spectra of the $NiCo_2O_4$/NiO@CNF composite showing the deconvoluted spectra of (C) Co 2p, (D) Ni 2p, (E) O 1 s, and (F) C 1 s.

characteristics of the fabricated materials were studied using XRD Fig. 1**A.** Pronounced XRD peaks in the low-angle region evidenced the crystalline nature of the NiCo-MOF, arising from the ordered coordination of Ni and Co ions with terephthalate linkers. After calcination at 550 °C, the characteristic MOF reflections completely disappeared and diffraction peaks corresponding to mixed oxide phases emerged, confirming the conversion of the MOF into $NiCo_2O_4$/NiO mixed. The characteristic diffraction peaks at 18.9°, 31.2°, 36.7°, 44.7°, 59.2°, and 65.1° are attributed to the cubic spinel structure of $NiCo_2O_4$, while the additional diffraction peaks at 43.3° and 62.7°, corresponding to the (200) and (220) planes, respectively, which confirm the presence of cubic NiO. The coexistence of these characteristic diffraction peaks confirms the formation of the $NiCo_2O_4$/NiO mixed oxide structure. The pristine CNF sample displayed a broad diffraction peak near 26°, corresponding to graphitic carbon plane of (002). After composite formation, all major diffraction peaks of $NiCo_2O_4$/NiO and CNF remained clearly visible in the composite without noticeable structural changes, confirming the successful incorporation of conductive CNFs while preserving the crystalline spinel structure [33].

The vibrational characteristics of the synthesized samples were further evaluated using Raman spectroscopy, as shown in Fig. 1**B**. The NiCo-MOF precursor exhibited several sharp and well-resolved vibrational bands centered near 300–650 cm^{-1}, corresponding to metal-oxygen coordination vibrations within the framework structure. In addition, distinct Raman bands observed around 820, 1000, 1180, 1280, 1390, and 1610 cm^{-1} are mainly associated with the vibrational modes of coordinated terephthalate linker. The bands near 1000–1650 cm^{-1} are mainly associated with aromatic ring and C–H vibrations. These characteristic features support the coordination of terephthalate linkers with Ni/Co metal centers and the formation of the NiCo-MOF structure. After calcination, these organic vibrational bands completely disappeared, indicating the decomposition and removal of the coordinated organic framework during thermal treatment. Raman analysis further revealed characteristic vibrational features of both $NiCo_2O_4$ and NiO. The Raman spectrum of $NiCo_2O_4$/NiO was separately fitted to resolve and better understand the overlapping Raman signals. The fitted Raman data was provided in the supporting information Fig S2. The band observed at approximately 336 cm^{-1} may be attributed to the defect activated one phonon transverse optical (1P-TO) mode of nanostructured NiO. The broad band at approximately 530 cm^{-1} is associated with the one-phonon longitudinal optical (1P-LO) vibration of NiO. However, this region also overlaps with the $F_{2\,g}$ vibration of spinel $NiCo_2O_4$. The broad band centered at approximately 1072 cm^{-1} is assigned to the second-order two-phonon longitudinal optical (2LO) mode of NiO. In addition, the Raman bands observed at approximately 198, 445, and 667 cm^{-1} are attributed to the $F_{2\,g}$, E_g, and $A_{1\,g}$ modes of spinel $NiCo_2O_4$, respectively. The coexistence of these characteristic $NiCo_2O_4$ and NiO vibrational features supports the formation of the $NiCo_2O_4$/NiOmixed-oxide structure [34,35]. Distinct Raman features at 1360 and 1580 cm^{-1} confirmed the presence of D and G bands, respectively. The D-band arises from the defect activated breathing mode of sp^2 aromatic rings whereas G-band originated from the in-plane $E_{2\,g}$ stretching vibration of sp^2-hybridized carbon atoms and other pronounced peak at 2673 cm^{-1} features second order double resonance Raman process and indicates the presence of ordered graphitic domains. The calculated (I_D/I_G) ratio of CNF is 0.125, indicating a relatively low defect density and a well-ordered graphitic structure. The Raman spectrum of $NiCo_2O_4$/NiO@CNF exhibited characteristic bands attributable to the graphitic CNF framework together with metal-oxide vibrational modes, providing evidence for the successful integration of $NiCo_2O_4$/NiO with CNF. Compared to bare CNF, the D-band, G-band and 2D-band peaks are shifted to 1342, 1572 and 2694 cm^{-1} in $NiCo_2O_4$/NiO@CNF, respectively. The I_D/I_G ratio increase from 0.125 (CNF) to 0.172 for $NiCo_2O_4$/NiO@CNF which indicate the defect induced disorder in graphitic carbon framework after the incorporation of $NiCo_2O_4$/NiO. The shift in the Raman signal suggests of appreciable interfacial interaction between $NiCo_2O_4$/NiO and CNF.

XPS measurements were performed to determine the elemental composition and valence states of the $NiCo_2O_4$/NiO@CNF composite Fig. 1 **(C–F)**. The Co 2p high resolution spectrum shown in Fig. 1**C** which exhibited major spin orbit splitting peaks centered at 780 (Co $2p_{3/2}$) and 795.2 eV (Co $2p_{1/2}$). Co 2p fitting revealed Co^{3+}/Co^{2+} components at 779.8/781.5 eV for Co $2p_{3/2}$ and 795.1/797.2 eV for Co $2p_{1/2}$, respectively which confirms mixed cobalt valence states and satellite features of Co 2p situated at 785.4 and 804.3 eV. The Ni 2p spectrum showed the characteristic Ni $2p_{3/2}$ and Ni $2p_{1/2}$ signals at 854.2 and 872.9 eV, with deconvolution confirming the coexistence of Ni^{2+} and Ni^{3+} species in both regions, accompanied by satellite features Fig. 1**D**. The coexistence of Ni^{2+}/Ni^{3+} and Co^{2+}/Co^{3+} states is characteristic of mixed-valence spinel $NiCo_2O_4$. The pronounced Ni^{2+} contribution is also consistent with the presence of NiO. Together with the XRD and Raman results, this XPS analysis further support the formation of $NiCo_2O_4$/NiO mixed oxide structure.

The O 1 s high-resolution XPS spectra have a peak at 529.7 eV was assigned to lattice oxygen associated with metal-oxygen bonding within the mixed oxide structure. The deconvoluted 531.2 eV corresponds to surface oxygen which includes surface hydroxyl species, chemisorbed oxygen, carbonyl-containing groups, and other undercoordinated surface oxygen species. The higher binding-energy peak observed around 533.4 eV was attributed to adsorbed oxygen species and surface oxygen containing functional groups in CNF Fig. 1**E** [36]. The C 1 s spectrum Fig. 1**F** showed peaks at 284.7, 285.1, 286.3, 289.4 and 291.2 eV corresponding to C═C, C–C, C–O, O–C═O/C═O and π- π* satellite peak, respectively. These oxygenated carbon groups strengthen the interfacial interaction between the spinel oxide and CNF surface [37].

3.2. FE-SEM morphological analysis

The morphology and microstructure of the fabricated materials were evaluated by FESEM, with representative images provided in Fig. 2 **(A–J)**. The NiCo-MOF exhibits a partially stacked, sheet like morphology with relatively smooth surfaces and well-defined edges (Fig. 2**A and B**). Pristine CNF showed a randomly entangled network of continuous submicron carbon fibers Fig. 2**C and D**. The fibers were uniformly distributed and formed an open three-dimensional architecture with numerous inter-fiber voids [38]. The FESEM images of the calcined $NiCo_2O_4$/NiO sample Fig. 2**E–G** revealed a distinctly different morphology. The material consisted of intercalated sheet like nanostructures assembled into larger microstructure aggregates. At higher magnification Fig. 2**F and G,** the oxide particles displayed rough surfaces with irregular edges and layered features. Calcination of the NiCo-MOF precursor facilitates organic ligand removal and reconstruction into crystalline mixed oxides. The rough surface texture generated during calcination increases the exposed surface region and creates numerous edge sites throughout the oxide structure. As shown in Fig. 2**H–J**, the $NiCo_2O_4$/NiO@CNF composite exhibits a homogeneous dispersion of oxide structures across the interconnected CNF network. Unlike the pristine oxide sample, severe particle aggregation was not observed in the composite, indicating that the CNFs effectively restricted the accumulation of oxide particles during composite formation. At higher magnification, the oxide nanosheets were seen closely attached to the carbon fibers, indicating effective contact between the two components. The oxide particles were anchored along the CNF surface, producing numerous oxide-carbon contact regions that can facilitate electron transport across the composite. In addition, the coexistence of conductive fibers and defect-rich oxide structures creates a hierarchical architecture with improved accessibility of active surface regions and shortened charge transfer pathways [39]. The elemental distribution of the prepared composite was examined by energy-dispersive X-ray spectroscopy (EDS) and elemental mapping analysis Fig. S3. EDS analysis detected only Ni, Co, O, and C, with no noticeable foreign elements, supporting the high elemental purity of the composite Fig. S3A. The

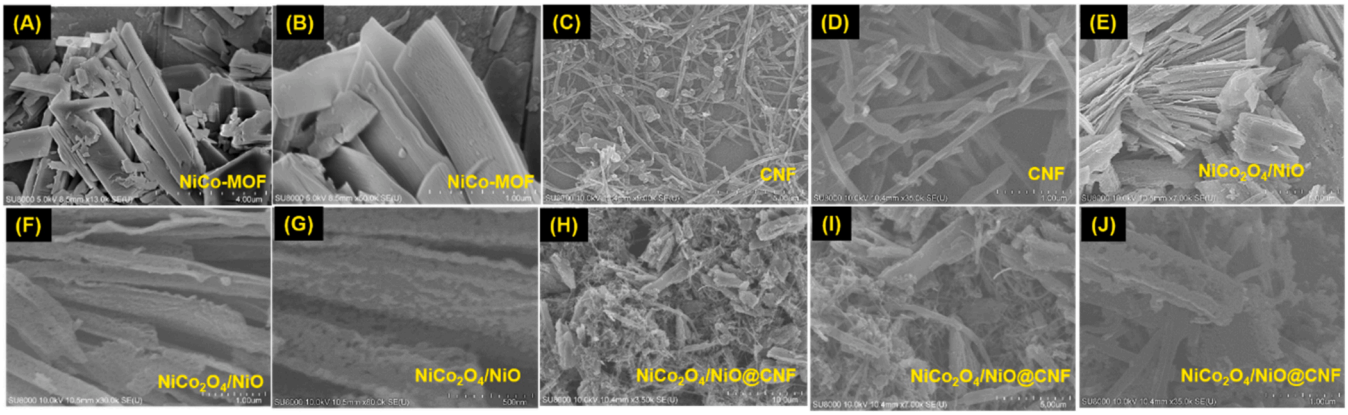


Fig. 2. FE-SEM micrographs of (A, B) CNF and (C–E) MOF-derived $NiCo_2O_4$/NiO at various magnifications, (F–H) FE-SEM images of the $NiCo_2O_4$/NiO@CNF composite at various magnifications, showing the uniform distribution and intimate integration of $NiCo_2O_4$/NiO microstructures on the CNF surface.

mapping results in Fig. S3**(B–F)** display a consistent spatial distribution of Ni, Co, O, and C, indicating well-dispersed spinel oxide throughout the CNF network. The uniform elemental distribution indicates close interfacial contact between $NiCo_2O_4$/NiO and CNF, facilitating charge transport during electrochemical sensing.

3.3. TEM morphological characterization

Fig. 3**(A–H)** presents TEM and HRTEM images that provide further insight into the nanoscale structural and crystallographic features of the synthesized materials. The $NiCo_2O_4$/NiO sample exhibits a nonuniform assembly of closely connected nanostructured regions Fig. (3**A and B)**. The oxide particles are closely packed and contain visible grain boundaries throughout the structure. This morphology agrees with the structural reconstruction during calcination, where removal of the organic ligands from the NiCo-MOF precursor leads to crystallized mixed oxide nanodomains. Well-defined lattice fringes in Fig. 3**C** verify the crystallinity of the $NiCo_2O_4$/NiO phase after calcination [40]. The TEM images of $NiCo_2O_4$/NiO@CNF Fig. 3**D–F** confirm the successful integration of oxide particles with carbon nanofibers. The CNFs are clearly visible as elongated fibrous structures, while the oxide particles are crumbled around the fiber surface. This local interfacial contact between oxide and carbon phases can reduce particle accumulation and improve electron movement from the oxide region to the conductive CNF support.

The HRTEM image of the composite also shows well-defined lattice fringes, indicating that the crystalline mixed oxide structure is preserved after CNF incorporation (Fig. 3**G**). The lattice fringes are consistent with the XRD-indexed planes of CNF- 0.34 nm (002), $NiCo_2O_4$ - 0.28 nm (220) and NiO- 0.21 nm (200) confirming that the composite formation. The SAED pattern shows both diffuse and well-defined diffraction rings, indicating the coexistence of carbonaceous and crystalline metal-oxide phases (Fig. 3H). The rings are indexed to the characteristic planes of CNF and $NiCo_2O_4$/NiO. Because some $NiCo_2O_4$ and NiO reflections have closely similar interplanar spacings, certain rings overlap and cannot be resolved separately in SAED.

3.4. Charge-Transfer Behavior and Electrochemical Activity

The electrochemical response of the fabricated electrodes was subsequently examined by CV using 5 mM $[Fe(CN)_6]^{3-/4-}$ in 0.1 M KCl at a scan rate of 50 mV s^{-1}. As presented in Fig. 4**A**, the bare SPCE exhibited a comparatively low current response without clearly identifiable redox peaks. Modification with CNF and NiCo-MOF altered the redox response, while the $NiCo_2O_4$/NiO showed higher anodic and cathodic peak currents. Among the tested electrodes, the $NiCo_2O_4$/NiO@CNF exhibited the highest redox peak currents (I_{pa} = 77.48 μA and I_{pc} = −72.02 μA). The enhanced current response of the composite is attributed to the combined electrochemical contribution of the $NiCo_2O_4$/Ni oxide and conductive CNF. Scan rate dependent CVs of $NiCo_2O_4$/

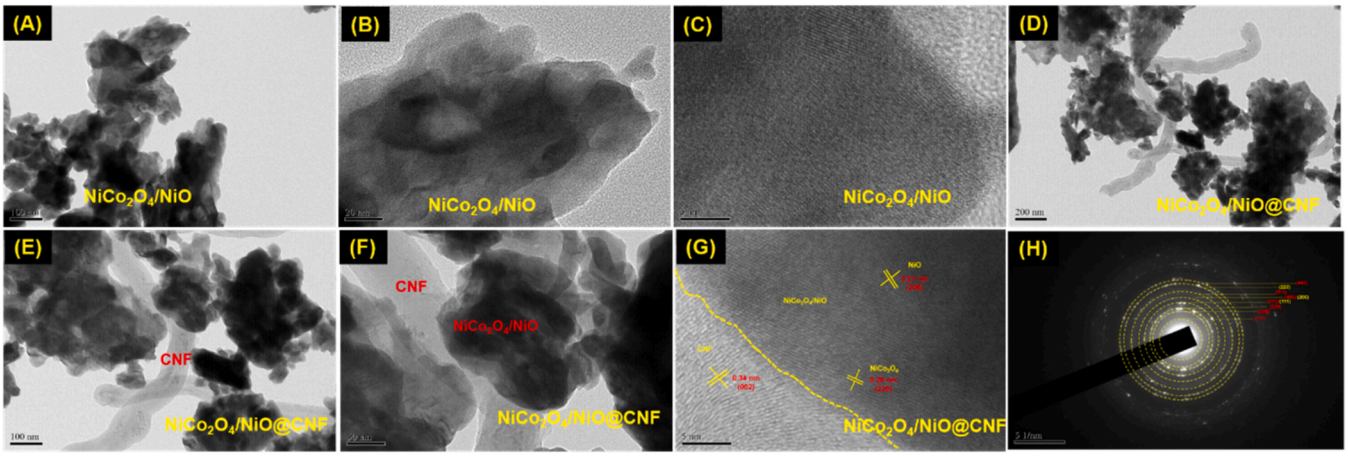


Fig. 3. TEM characterization of the synthesized materials. (A, B) TEM images of MOF-derived $NiCo_2O_4$/NiO, revealing aggregated oxide nanostructures, (C) HRTEM image of $NiCo_2O_4$/NiO showing well-resolved lattice fringes, (D–F) TEM images of the $NiCo_2O_4$/NiO@CNF composite at different magnifications, (G) HRTEM image of the $NiCo_2O_4$/NiO@CNF composite displaying distinct lattice fringes corresponding to the crystalline oxide and carbon phase and (H) SAED analysis of $NiCo_2O_4$/NiO@CNF displaying distinct diffraction rings associated with polycrystallinity.

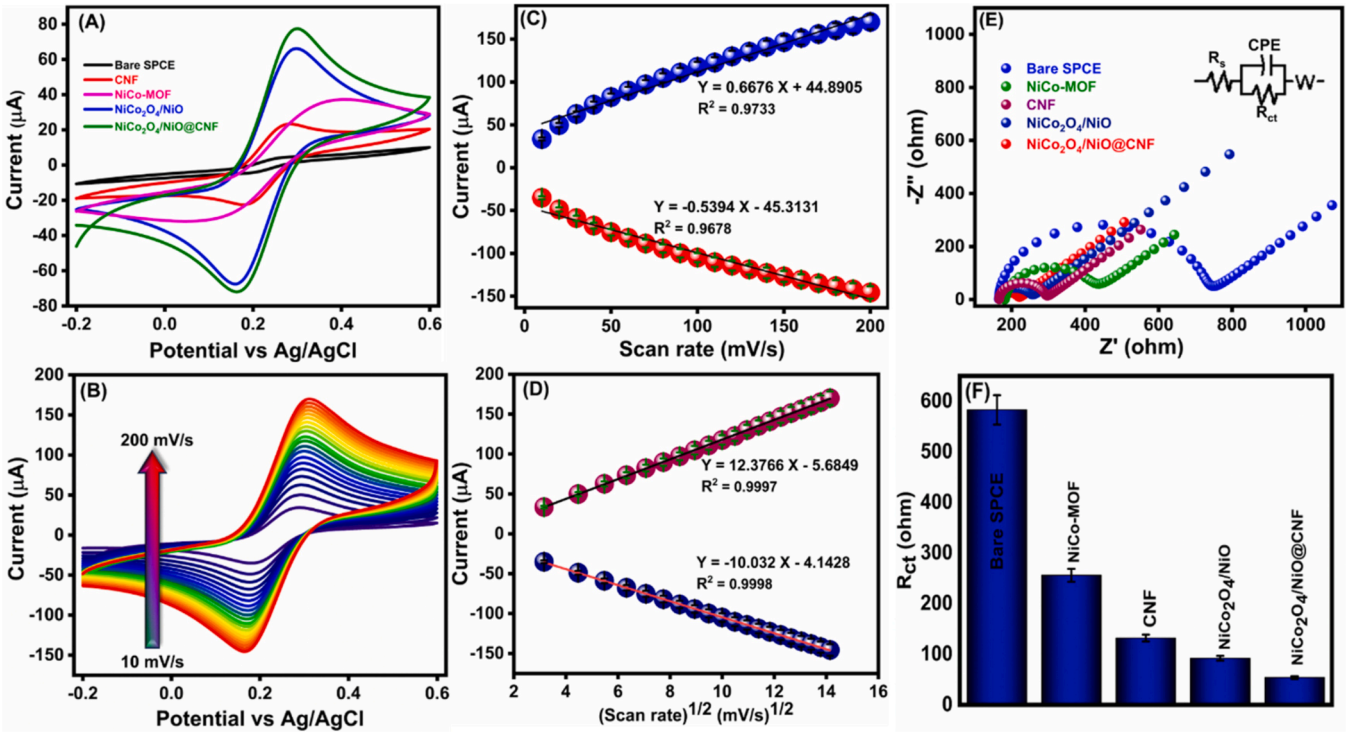


Fig. 4. Electrochemical characterization of the fabricated electrodes. (A) CV responses of bare and modified SPCEs in redox solution. (B) CVs of $NiCo_2O_4$/NiO@CNF/SPCE at scan rates of 10–200 mV s^{-1}. (C, D) Variation of anodic and cathodic peak currents with scan rate and its square root, respectively. (E) EIS Nyquist plots of the electrodes (inset: enlarged high-frequency region). (F) Comparison of fitted charge-transfer resistance (R_{ct}) values.

NiO@CNF/SPCE (10–200 mV s^{-1}) showed progressively enhanced redox peak currents while preserving distinct oxidation and reduction features Fig. 4**B.** Fig. 4**C** reveals a nearly linear variation of both oxidation and reduction peak currents with scan rate which givesR^2 values of 0.9733 and 0.9678, respectively. To investigate the role of mass-transfer diffusion, i_{pa} and i_{pc}were plotted as a function of the $v^{1/2}$ Fig. 4**D**and the near-unity R^2 values of 0.9997 and 0.9998 suggest that the redox reaction is mainly controlled by diffusion. The observed linearity reflects efficient diffusion and consistent redox behaviour. The apparent electroactive surface area for bare and other modified electrode was calculated from the Randles–Sevcik relation **Eq-S1.**

The calculated apparent electroactive surface area values are summarized in Table 1. The NiCo-MOF modified SPCE exhibited a large peak to peak separation (ΔEp ≈ 300 mV), indicating sluggish electron transfer kinetics. Therefore, it was excluded from the apparent electroactive surface area calculation using the conventional Randles–Sevcik equation. A continuous increase in electroactive area was observed after each modification step, with $NiCo_2O_4$/NiO@CNF/SPCE exhibiting the highest value of 0.0934 cm^2. A higher active surface area promotes greater electrolyte accessibility and exposes more electrochemically active sites.

The electron-transfer properties of the modified electrodes were evaluated by EIS using 5 mM $[Fe(CN)_6]^{3-/4-}$ in 0.1 M KCl as the electrolyte. Measurements were performed over a frequency range of 100 kHz to 0.1 Hz with an AC amplitude of 0.01 V and a DC bias of 0.20 V. The high-frequency arc corresponds to interfacial electron transfer, while the inclined low-frequency region is associated with diffusion processes. EIS fitting was performed with a Randles circuit model, shown in the inset of Fig. 4**E.** Bare SPCE exhibited the most pronounced semicircular response, with an R_{ct} value of 583 Ω. Among the modified electrodes, NiCo-MOF exhibited a relatively high R_{ct} of 256 Ω. This higher resistance can be attributed to the presence of insulating organic ligands within the MOF framework, which restrict efficient electron transport across the electrode surface. Following thermal conversion, the R_{ct} value decreased markedly to 92 Ω for the $NiCo_2O_4$/NiO modified electrode. The minimum charge-transfer resistance of 54 Ω was obtained for $NiCo_2O_4$/NiO@CNF, demonstrating the beneficial role of the conductive CNF network in facilitating electron transport. The substantial reduction in R_{ct} confirms that the CNF network provides direct pathways for electron transport while simultaneously improving electrical communication between neighboring oxide domains. Fig. 4**F** the overall charge-transfer behavior follows the order: Bare SPCE > NiCo-MOF > CNF > $NiCo_2O_4$/NiO > $NiCo_2O_4$/NiO@CNF. The interfacial charge-transfer kinetics were further evaluated by determining the apparent heterogeneous electron transfer rate constant (k_{app}) according to Eq. S2. A gradual increase in the k_{app} values was observed from 4.66×10^{-4} cm s^{-1} for NiCo-MOF/SPCE to 5.03×10^{-3} cm s^{-1} for $NiCo_2O_4$/NiO@CNF/SPCE Table 2. The higher k_{app} value indicates enhanced interfacial electron transfer kinetics, which can be attributed

Table 1
Electrochemical parameters obtained from CV measurements.

Electrode	Ipa (μA)	Ipc (μA)	Apparent Electroactive surface area (cm^2)
Bare SPCE	4.85	-4.47	0.0059
CNF/SPCE	25.57	-23.45	0.0308
$NiCo_2O_4$/NiO/SPCE	66.09	-67.39	0.0797
$NiCo_2O_4$/NiO@CNF/SPCE	77.42	-72.30	0.0934

Table 2
Summary of electrochemical parameters derived from EIS analysis.

Electrode	R_{ct} (Ω)	K_{app} (cm s^{-1})
Bare SPCE	583	4.66×10^{-4}
NiCo-MOF/SPCE	256	1.06×10^{-3}
CNF/SPCE	132	2.06×10^{-3}
$NiCo_2O_4$/NiO/SPCE	92	2.95×10^{-3}
$NiCo_2O_4$/NiO@CNF/SPCE	54	5.03×10^{-3}

to the synergistic combination of electroactive $NiCo_2O_4$/NiO sites and the conductive CNF network. Combined results from EIS, CV, k_{app} calculation, and apparent electroactive surface area estimation consistently demonstrate that the MOF-derived $NiCo_2O_4$/NiO@CNF composite possesses good conductivity, faster charge transfer kinetics, and enhanced electrochemical activity compared with the individual components.

3.5. Proposed Reaction Mechanism for VLN Oxidation

The proposed electrochemical oxidation pathway of VLN at the $NiCo_2O_4$/NiO@CNF electrode is illustrated in Scheme 2. Based on the reported electrochemical behavior of VLN, oxidation is proposed to involve the phenolic/methoxy functionality, with formation of an oxidized intermediate followed by the participation of water and release of methanol. The oxidation peak potential shifted toward less positive values with increasing pH, indicating that proton transfer is involved in the electrochemical process. However, because VLN oxidation is irreversible and the investigated pH range extends across its acid–base transition, the observed pH dependence is not used to assign a specific proton to electron stoichiometry. Furthermore, the oxidation products were not independently identified in the present study. Therefore, the reaction pathway shown in Scheme 2 is presented as a proposed mechanism based on previously reported VLN electrochemistry rather than as a confirmed reaction sequence [14].

3.6. Effect of Electrode Modification

The bare SPCE exhibited a relatively weak VLN oxidation response. Modification with NiCo-MOF and CNF increased the oxidation response compared with the bare electrode, with both electrodes showing comparable current responses. The $NiCo_2O_4$/NiO modified electrode exhibited a further increase in the VLN oxidation current. Among the investigated electrodes, $NiCo_2O_4$/NiO@CNF/SPCE showed the highest oxidation response, indicating that the combination of $NiCo_2O_4$/NiO and conductive CNF provides a favourable electrode surface for VLN sensing (Fig. 5**A**). The anodic peak potentials remained within a relatively narrow potential range for the different electrodes, indicating that the principal improvement was observed in the magnitude of the sensing response rather than a substantial shift in the VLN oxidation potential. A cathodic feature observed during the reverse scan originated from the redox nature of NiCo2O4/NiO and it isn't originated from the electroactive species of VLN. The corresponding oxidation current comparison is presented in Fig. 5**B**. As presented in Fig. 5**C**, the effect of $NiCo_2O_4$/Co_3O_4@CNF amount was evaluated using different amount between 20.4, 40.8, 61.2, and 81.6 μg cm^{-2} corresponding to catalyst ink volumes of 2, 4, 6, and 8 μL, respectively. The oxidation signal progressively increased with catalyst quantity, reaching its highest value at 61.2 μg cm^{-2}. At 81.6 μg cm^{-2} the oxidation current declined, because of the thicker catalyst layer restricted electron transfer and impeded VLN diffusion toward the electrode surface. Accordingly, 61.2 μg cm^{-2} (6 μL) was selected as the optimal catalyst loading and employed for all further electrochemical measurements.

3.7. Effect of Composite Composition

To optimize the composition of the sensing material, different $NiCo_2O_4$/NiO@CNF mass ratios of 1:1, 1:2, and 2:1 was investigated Fig. 5**D.** The electrochemical response was strongly influenced by the relative amount of oxide and CNF. Although the 1:2 composition exhibited a higher absolute current, it also produced a substantially higher background current and a less defined oxidation feature. In comparison, the 1:1 composition showed a more distinct VLN oxidation peak with a better-resolved response relative to the background. Increasing the oxide content to a 2:1 ratio resulted in a weaker electrochemical response. Therefore, considering the baseline-corrected VLN oxidation response rather than the absolute current alone, the 1:1 mass ratio was selected as the optimum composition for subsequent experiments.

3.8. Effect of pH

As illustrated in Fig. 5**E**, the effect of pH on the electrochemical response of VLN was investigated over the pH range of 3–8. The anodic oxidation current increased with increasing pH up to pH 7 and subsequently decreased at pH 8. At higher pH, particularly pH 7–8 the oxidation feature became broader and less well defined. This behavior may be associated with the acid-base properties of VLN, since the investigated pH range extends across its reported pKa (~7.4), where changes in protonation state can influence its electrochemical response. Considering the anodic oxidation response and the practical near-neutral sensing condition, pH 7 was selected for subsequent experiments. The corresponding current responses obtained at different pH values are provided in Supplementary Fig. S4.

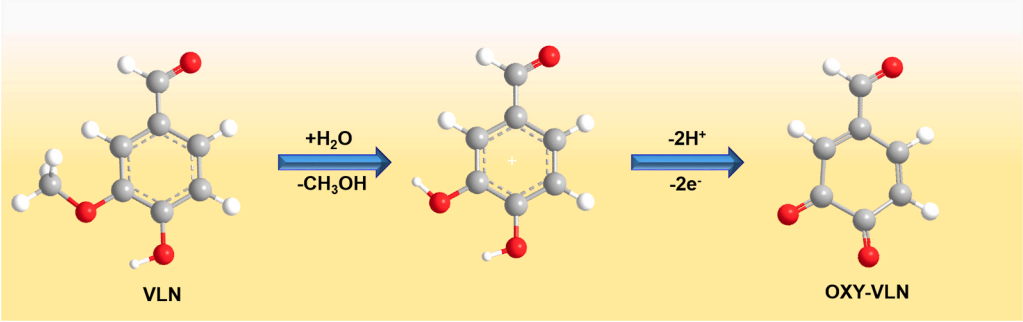
As shown in Fig. 5**F**, the oxidation peak potential shifted toward less positive potentials with increasing pH and followed the linear relationship [41].

$$E_{pa} = -0.0476\,pH + 0.8879 \quad (2)$$

The linear fit (R^2=0.9808) and the negative slope of 47.6 mV pH^{-1} confirms that the oxidation potential of VLN is dependent on solution pH and indicates the involvement of proton transfer in the oxidation process. However, because VLN oxidation at the $NiCo_2O_4$/NiO@CNF electrode is irreversible, the observed slope is not interpreted using the reversible Nernst equation and is not used to determine a specific proton to electron stoichiometry. Therefore, the pH dependent potential shift is considered evidence of proton involvement rather than quantitative confirmation of a particular proton coupled electron transfer ratio.

3.9. Cyclic Voltammetric response toward VLN

CV was employed to evaluate the oxidation characteristics of VLN in



Scheme 2. Schematic representation of the proposed VLN oxidation route on $NiCo_2O_4$/NiO@CNF.

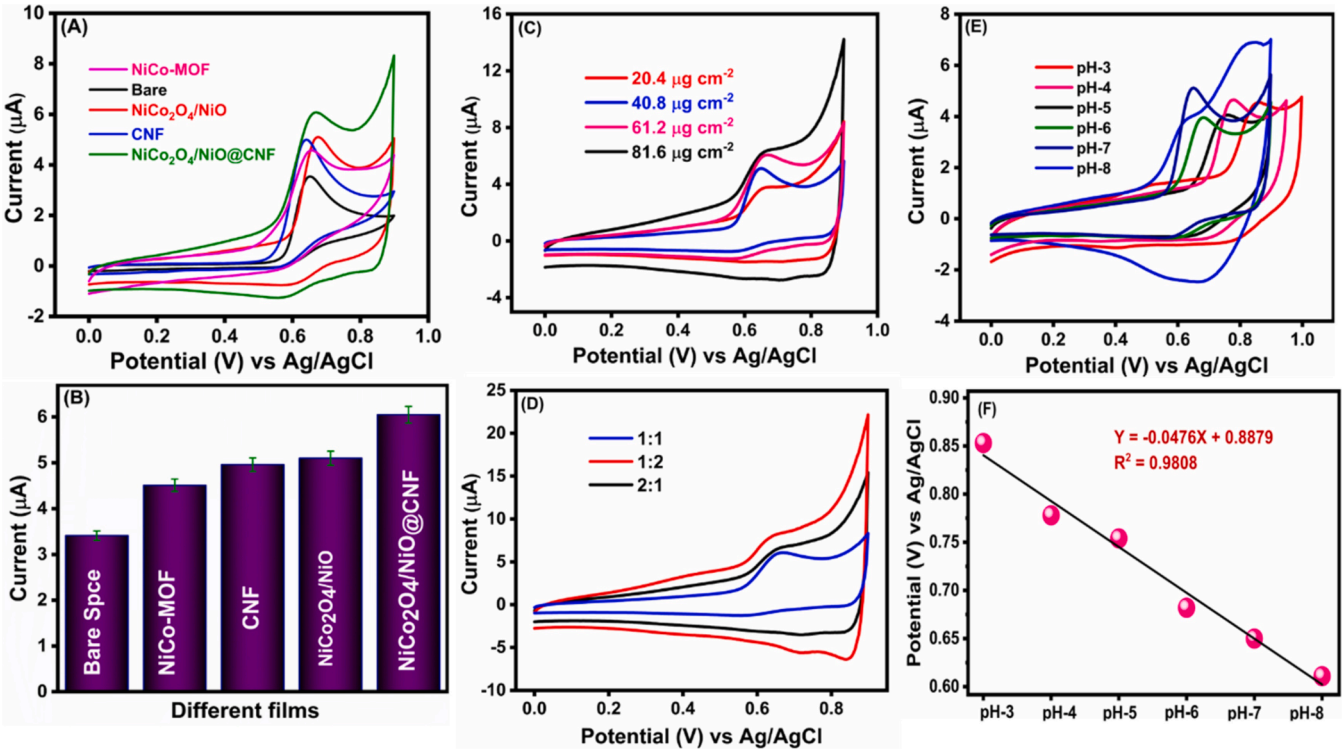


Fig. 5. Optimization of experimental parameters for VLN determination at the $NiCo_2O_4$/NiO@CNF-modified electrode. (A) CV recorded at bare SPCE, NiCo-MOF/SPCE, $NiCo_2O_4$/NiO/SPCE, CNF/SPCE, and $NiCo_2O_4$/NiO@CNF/SPCE in the presence of 50 μmol L^{-1} VLN. (B) Comparative anodic peak-current responses of VLN at various modified electrodes. (C) Influence of catalyst loading on the electrochemical oxidation response of 50 μmol L^{-1} VLN. (D) Effect of different $NiCo_2O_4$/NiO@CNF mass ratios 1:1, 1:2, and 2:1 on the oxidation response. (E–F) Effect of solution pH (3–8) on 50 μmol L^{-1} VLN and the corresponding linear dependence of anodic peak potential (E_{pa}) on pH.

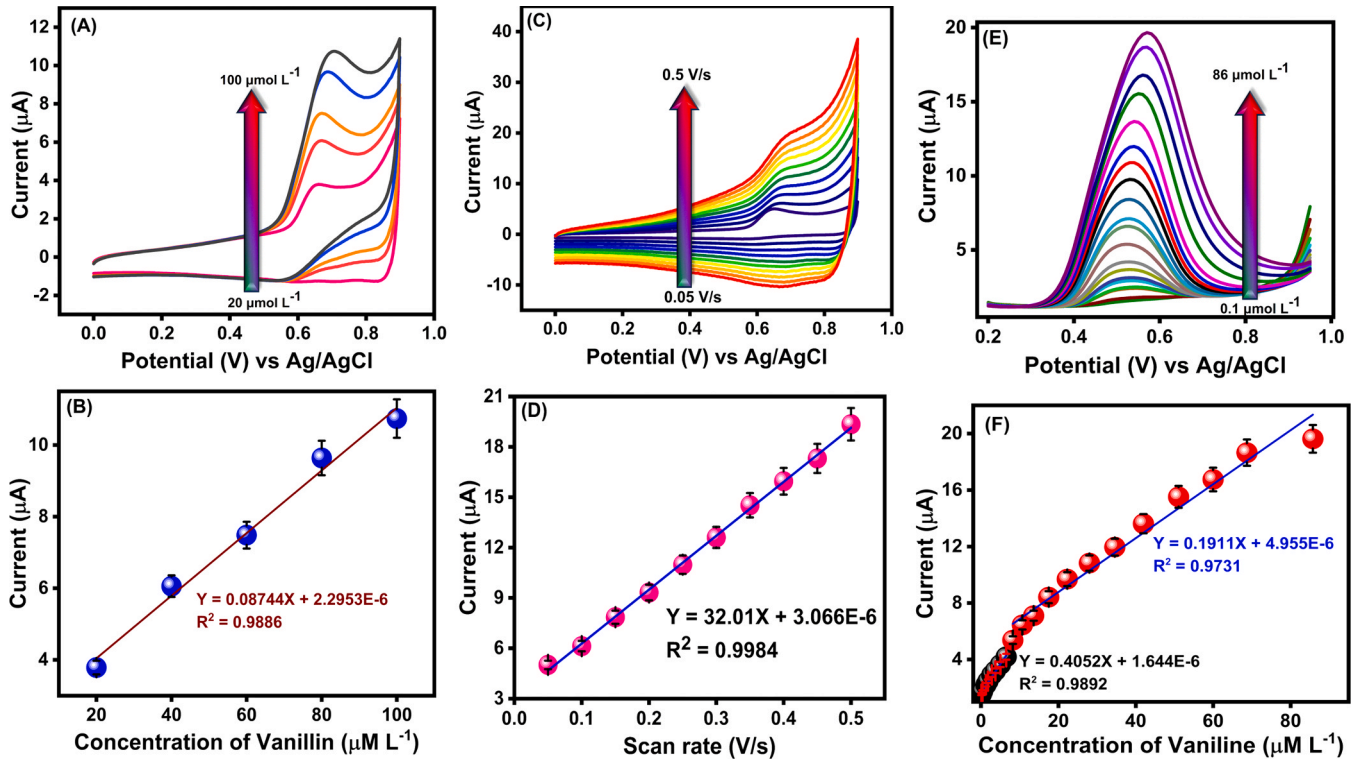


Fig. 6. Electrochemical determination of VLN at the $NiCo_2O_4$/NiO@CNF modified electrode. (A) CV responses recorded at different concentrations of VLN, (B) Relationship between VLN concentration and oxidation peak current obtained using CV, (C) CV of the $NiCo_2O_4$/NiO@CNF electrode recorded at different scan rates ranging from 0.05 to 0.50 V s^{-1} at 50 μmol L^{-1} of VLN, (D) Linear dependence of peak oxidation current on scan rate, (E) DPV responses obtained at various VLN concentrations and (F) Corresponding calibration plots showing the two linear concentration ranges for VLN determination.

different concentration at the $NiCo_2O_4$/NiO@CNF/SPCE with the resulting profiles shown in Fig. 6**A**. A progressive increase in oxidation peak current was observed as the VLN concentration rose from 20 to 100 μM, while the well-defined voltammetric profiles were retained, indicating efficient and stable electrocatalytic oxidation at the modified electrode. The increase in peak current reflects the greater availability of VLN molecules participating in the oxidation process at the electrode interface. In addition, the symmetrical oxidation peaks suggest rapid electron-transfer kinetics and efficient interaction between VLN and the $NiCo_2O_4$/NiO@CNF surface. Fig. 6**B** demonstrates a good linear correlation between VLN concentration and the corresponding oxidation current [42].

3.10. Different scan rate analysis

To elucidate the kinetic behavior of VLN oxidation, CV profiles were collected at different scan rates from 0.05 to 0.50 V s^{-1}, with the results presented in Fig. 6**C**. Higher scan rates produced larger oxidation currents, indicating fast interfacial electron-transfer processes. Simultaneously, the oxidation peak potential shifted gradually toward more positive potentials, suggesting that the oxidation process is electrochemically irreversible. A highly linear correlation between the oxidation peak current and scan rate was obtained, as evidenced by an R^2 value of 0.9984 Fig. 6**D**. To further evaluate the kinetic characteristics of the electrochemical process, a log (i_p) vs log (v) plot was constructed which exhibited a b-value of 0.61 Fig. S5. This value indicates that VLN detection at the modified electrode is not completely surface controlled but instead involves mixed diffusion and surface controlled contributions, with a relatively stronger diffusion contribution. E_{pa} was plotted as a function of $\log_{10}\nu$ and analysed according to Laviron's theory for irreversible electrode reactions. The regression analysis plotted with a linear equation of $E_{pa} = 0.0357 \log_{10}\nu + 0.6934$ (R^2 =0.9212). Using the Laviron slope relationship Eq. S3 **& S4**, the apparent charge-transfer coefficient product, (1 − α)n, was estimated to be 1.66 at 298 K. [43]. Since the number of transferred electrons cannot be independently determined from the same Laviron relationship, *n* was not calculated from these equations. When n = 2 is considered based on the proposed VLN oxidation pathway reported in the literature, the corresponding transfer coefficient α is estimated to be 0.171. The electrochemical response exhibited mixed diffusion and surface-controlled characteristics and the formal potential could not be independently determined, so the standard heterogeneous electron transfer rate constant was not calculated.

3.11. Quantification analysis of VLN

For more sensitive detection, DPV measurements were performed at different VLN levels, and the corresponding current profiles are displayed in Fig. 6**E**. DPV analysis was performed in pH 7 phosphate buffer over a potential window of 0.2–1.0 V, using a pulse amplitude of 0.1 V, a pulse time of 0.02 s, and a scan rate of 0.025 V s^{-1} . A steady increase in oxidation peak current with VLN concentration was observed, indicating efficient electrocatalytic response and good analytical performance of the $NiCo_2O_4$/NiO@CNF-modified electrode. The well-defined oxidation peaks and stable baseline current indicate signal reproducibility and efficient charge-transfer characteristics. The linear relationship between VLN concentration and oxidation peak current is shown in Fig. 6**F**, revealing two distinct linear concentration ranges. The first linear range spanned 0.10–6.50 μmol L^{-1}, with a correlation coefficient of R^2= 0.9892. At higher concentrations, a second linear relationship was observed from 8.23 to 86 μmol L^{-1} with R^2 = 0.9731.

The observed concentration dependent response may be attributed to changes in the availability of electroactive sites and mass transport as the VLN concentration increases. At lower concentrations, the electrode exhibits higher sensitivity, resulting in a steeper calibration slope. At higher VLN concentrations, the reduced sensitivity may be associated with changes in surface-site availability and interfacial reaction kinetics. The combined influence diffusion/surface-controlled behaviour may contribute to the observed differences in the electrode response between the lower and higher concentration regions. The low concentration calibration region was used to estimate the LOD and sensitivity of electrode. The LOD value was estimated using a LOD= 3σ/s, σ is standard deviation of response and s is the sensitivity of electrode. The sensitivity of the electrode was calculated from the slope value obtained from the low concentration linear calibration curve and geometrical surface area of the SPCE working electrode (0.196 cm^2). The calculated sensitivity and LOD values were 2.07 μA μM^{-1} cm^{-2} and 6.65 nmol L^{-1}, respectively. The mathematically calculated LOD value is lower than the lowest experimental tested concentration of VLN (0.1 μM), therefore this LOD value considered as an estimated analytical detection limit rather than experimental tested concentration [41]. The $NiCo_2O_4$/Co_3O_4@CNF electrode exhibited a low LOD together with a useful linear range and high sensitivity, demonstrating its potential as an effective sensing platform for VLN analysis and food safety assessment. For practical food analysis, the working concentration range is more relevant than the lowest achievable detection limit. Based on the extraction and dilution procedure used in this study, VLN is expected to be present in the micromolar range in the final test solution. Example, a food product containing 100 mg kg^{-1} VLN would correspond to 33 μmol L^{-1} under the present sample-preparation conditions, which falls within the second linear range of the sensor 8.23–86 μmol L^{-1}. Thus, the LOD of 6.65 nmol L^{-1} represents the lower analytical capability of the sensor rather than a concentration specifically required for routine food analysis. More importantly, the working range covers the micromolar concentrations relevant to the analysis of the prepared food extracts.

Table 3 compares the analytical performance of the proposed $NiCo_2O_4$/NiO@CNF sensor with previously reported electrochemical platforms for VLN determination.

3.12. Selectivity, stability, reproducibility on VLN sensing

The ability of the $NiCo_2O_4$/NiO@CNF modified electrode to selectively detect VLN was assessed against representative inorganic ions, sugars, and electroactive species commonly found in food matrices. The corresponding DPV responses of 25 μM L^{-1} of VLN are presented in Fig. 7**A** with 15-fold higher potential common interfering species including citric acid (CA), Co^{2+}, Fe^{2+}, fructose, glucose, sucrose, Mg^{2+}, Na^+, K^+, and Cl^- were individually introduced into the electrolyte containing VLN. The oxidation peak of VLN remained nearly unchanged after the addition of these species, indicating negligible interference toward the sensing response. Although carbohydrates and metal ions are frequently present in food matrices, they do not undergo significant oxidation within the investigated potential window and therefore contribute minimally to the electrochemical signal. All examined interfering species caused 10 – 15% change in the current response, indicating good resistance to common interference samples. The comparative current responses and corresponding bar diagram is presented in Fig. S7A**,** with all measurements performed in triplicate (n = 3).

Five independently fabricated $NiCo_2O_4$/NiO@CNF electrodes were examined under identical conditions to determine sensor reproducibility Fig. 7**B.** All electrodes generated nearly identical oxidation currents with only minor variations in peak intensity, indicating excellent fabrication consistency and uniform distribution of the active material on the electrode surface. The calculated relative standard deviation (RSD) was 3.34%, confirming satisfactory reproducibility of the fabrication process. The good reproducibility likely originates from the well-dispersed oxide particles in the CNF framework together with the stable catalyst ink formulation. The corresponding current comparison and statistical analysis are provided in Supplementary Fig. S7**-B.**

As shown in Fig. 7**C**, the storage stability of the $NiCo_2O_4$/NiO@CNF modified SPCE was evaluated over 28 days by monitoring its

Table 3
Comparative analysis of various reported electrochemical sensing of VLN.

S no	Electrode material	Sensing method	Linear range (μmol L^{-1})	LOD (nM)	Sensitivity (μA.μM^{-1}.cm^{-2})	Reference
1	xGnP-AuNPs-$Ti_3C_2T_x$/GCE	DPV	0.1–8.5	29	_	[44]
2	MWCNT/GCE	AdDPV	4.15–294.12	8.51	_	[45]
3	Au/F-rGO/GCE	DPV	1 – 150	150	_	[46]
4	$BaFe_{12}O_{18}$@carbon black/SPCE	DPV	0.5–1084	396	1.216	[47]
5	SMM/Au@ZIF-67/ CPE	DPV	0.001–10	0.3	_	[48]
6	Bi_2S_3/SPCE	DPV	0.001–99	7	0.6	[49]
7	f-MWCNTs-FNTs/CPE	DPV	0.05 – 100	35	_	[50]
8	C-LFNO/GCE	i-t	0.008–0.36	11	_	[51]
9	$MnMoO_4$@f-CNF/RDE	i-t	1.25–487.5 & 587.5 –1500	27	0.266	[52]
10	Ni_3S_4/Co_3S_4-ErGO/GCE	SDLSV	0.02–20	0.8	_	[53]
11	$Mn_{0.5}Ni_{0.5}Co_2O_4$/g-C_3N_4@CeO_2/GCE	DPV	0.006–0.4; 1–1000	6.0	_	[54]
12	$NiCo(OH)_2$/rGO/GCE	SWV	0.005–0.14	6.1	_	[55]
13	Zr-UiO-66 MOF/GSPE	DPV	0.1–238	30		[56]
14	**MOF derived $NiCo_2O_4$/NiO@CNF/SPCE**	**DPV**	**0.10–6.50 & 8.23–86**	**6.65**	**2.07**	**Our work**

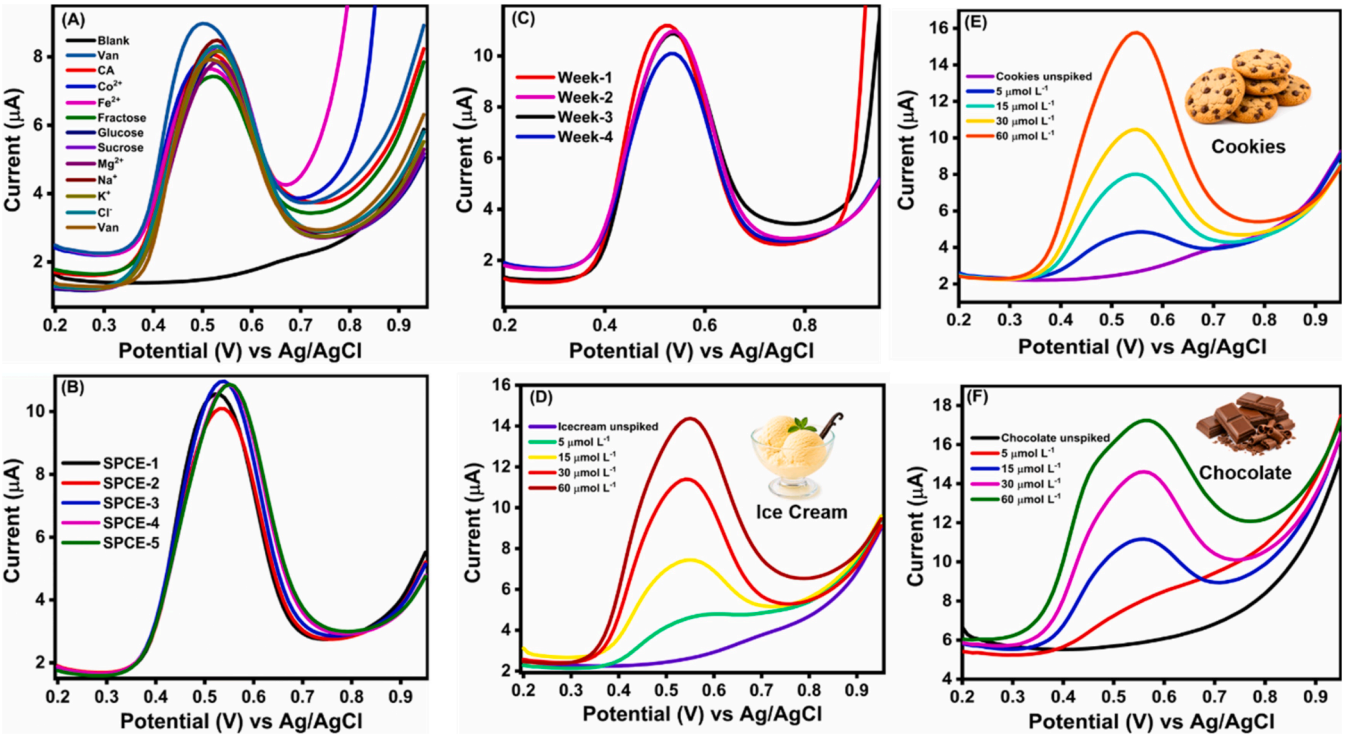


Fig. 7. Selectivity, stability, reproducibility, and real sample analysis of the $NiCo_2O_4$/NiO@CNF modified electrode toward VLN determination. (A) DPV profiles recorded with different common interferents, demonstrating the selective response of the sensor toward VLN. (B) Reproducibility study performed using five independently fabricated $NiCo_2O_4$/NiO@CNF modified SPCEs under identical experimental conditions. (C) Stability analysis fabricated sensor (D–F) DPV responses obtained from real sample analysis in commercial food matrices: (D) ice cream, (E) cookies and (F) chocolate.

electrochemical response toward VLN. After four weeks, the sensor retained approximately 95.58% of its initial current response, corresponding to a current loss of only 4.42%. This relatively small decrease in current indicates satisfactory storage stability of the developed sensing platform. The corresponding current retention results are presented in Fig. S7C. The slight reduction in current response during storage may associated with changes in the electrode surface or sensing layer over time. Nevertheless, the sensor maintained most of its initial response throughout the investigated storage period, supporting its suitability for practical VLN determination.

To further examine possible changes in the sensing material after electrochemical measurements, Raman spectra of $NiCo_2O_4$/NiO@CNF were recorded before and after VLN sensing, as presented in Fig. S7D. The characteristic Raman bands associated with the oxide and CNF components remained observable after electrochemical measurements, without noticeable changes in their positions. These observations suggest that no major changes in the Raman detectable structural features occurred during the sensing procedure. Minor variations in band intensity may arise from changes in the electrode surface following VLN oxidation. However, Raman spectroscopy alone cannot establish complete structural or chemical stability. Considering that VLN determination involves relatively short electrochemical measurements rather than prolonged electrocatalytic operation, the Raman comparison was included as supplementary evidence of material preservation under the investigated sensing conditions [17].

3.13. Real Sample Analysis

The practical performance of the sensor was evaluated using commercial ice cream, cookies, and chocolate samples. Before measurement,

the samples were processed to produce clarified extracts suitable for sensing [42]. 1 g of ice cream was dispersed in 20 mL deionized water, sonicated for 20 min, and filtered through a 0.22 μm membrane. For cookies and chocolate, 1 g of powdered sample was extracted with 20 mL ethanol/water (1:1, v/v) by sonication for 30 min. After centrifugation and 0.22 μm filtration, the clear extracts were diluted with phosphate buffer. VLN recovery was evaluated by spiking 5–60 μM and recording the corresponding DPV responses.

As shown in Fig. 7**D–F**, only insignificant background currents were observed for the unspiked samples, demonstrating minimal matrix interference. Following the addition of VLN, a well-defined oxidation peak appeared near the characteristic VLN oxidation potential and increased systematically with increasing concentration. The gradual increase in peak current demonstrates efficient oxidation of VLN even in the presence of complex food constituents such as sugars, fats, proteins, and flavouring compounds. The ice-cream sample Fig. 7**D** exhibited a clear concentration-dependent response with increasing oxidation current after each standard addition. Similar behavior was observed for cookies Fig. 7**E** and chocolate samples Fig. 7**F,** confirming the ability of the sensor to operate reliably in food matrices with substantially different compositions. The successful detection of VLN in these samples demonstrates the excellent matrix tolerance of the $NiCo_2O_4$/NiO@CNF modified electrode. The real-sample recovery data are summarized in Table S1, with recoveries ranging from 95% to 100% and RSD values below 2.5%. The method showed good precision, as indicated by the low RSD values, together with reliable accuracy based on the recovery results. These findings demonstrate that the $NiCo_2O_4$/NiO@CNF sensor can accurately determine VLN in complex food samples without significant matrix interference. The excellent analytical performance observed in real food samples can be attributed to the fast electron transfer characteristics of the mixed spinel oxide phase together with the conductive CNF framework, which collectively facilitate efficient charge transport and stable oxidation of VLN at the electrode interface. The results demonstrate the practical applicability of the developed sensing platform for routine food-quality monitoring, process control, and safety assessment of flavouring additives.

4. Conclusion

A MOF-derived $NiCo_2O_4$/NiO oxide combined with CNF was successfully prepared and employed as an electrode material for the electrochemical determination of VLN. The NiCo-MOF precursor was converted into $NiCo_2O_4$/NiO through calcination, followed by its combination with conductive CNF to improve the electrochemical sensing response. The $NiCo_2O_4$/NiO@CNF modified SPCE exhibited higher VLN oxidation current than the individual electrode materials, demonstrating the benefit of combining the mixed oxide with CNF. The optimized sensor exhibited two linear concentration ranges of 0.10–6.50 and 8.23–86 μmol L^{-1}, with a sensitivity of 2.07 μA μM^{-1} cm^{-2} and a LOD of 6.65 nmol L^{-1}. The sensor also showed satisfactory reproducibility with RSD of 3.34% and retained approximately 95.58% of its initial current response after 28 days of storage. Raman measurements before and after sensing showed no noticeable changes in the characteristic vibrational bands, suggesting that the major Raman detectable features of the sensing material were maintained during electrochemical measurements. Furthermore, the practical applicability of the proposed sensor was evaluated using VLN spiked commercial ice cream, cookie and chocolate samples, with recoveries ranging from 95% to 100%. These results indicate that the MOF-derived $NiCo_2O_4$/NiO@CNF material provides a useful electrode platform for VLN determination in real time food samples.

CRediT authorship contribution statement

P. Varatharajan: Writing – review & editing, Writing – original draft, Software, Resources, Methodology, Formal analysis, Data curation. **Kumar Gokulkumar:** Writing – review & editing, Writing – original draft, Visualization, Software, Resources, Methodology, Data curation. **Neeraja Bose:** Writing – review & editing, Writing – original draft. **Shih-Hsuan Chen:** Software, Resources. **Kun-Mu Lee:** Writing – review & editing, Writing – original draft, Validation, Methodology, Investigation, Funding acquisition, Formal analysis, Conceptualization.

Declaration of Competing Interest

The authors declare that they have no known competing financial interests or personal relationships that could have appeared to influence the work reported in this paper.

Acknowledgment

The authors thank the support from the National Science and Technology Council, Taiwan (Grant Number: 115–2221-E-182–048-MY3, 115–2221-E-182–047-MY2, 115–2221-E182–052), Chang Gung University, Taoyuan, Taiwan (URRPD2R0011).

Appendix A. Supporting information

Supplementary data associated with this article can be found in the online version at doi:10.1016/j.jallcom.2026.191984.

References

[1] N.J. Walton, M.J. Mayer, A. Narbad, Vanillin, Phytochemistry 63 (5) (2003) 505–515.
[2] M. Fache, B. Boutevin, S. Caillol, Vanillin production from lignin and its use as a renewable chemical, ACS Sustain. Chem. & Eng. 4 (1) (2016) 35–46.
[3] B. Kaur, D. Chakraborty, Biotechnological and molecular approaches for vanillin production: a review, Appl. Biochem. Biotechnol. 169 (4) (2013) 1353–1372.
[4] D.J. Fitzgerald, et al., Structure− function analysis of the vanillin molecule and its antifungal properties, J. Agric. Food Chem. 53 (5) (2005) 1769–1775.
[5] A. Olatunde, et al., Vanillin: A food additive with multiple biological activities, Eur. J. Med. Chem. Rep. (5) (2022) 100055.
[6] J. Burri, et al., Vanillin: more than a flavouring agent—a potent antioxidant, J. Sci. Food Agric. 48 (1) (1989) 49–56.
[7] A.K. Sinha, U.K. Sharma, N. Sharma, A comprehensive review on vanilla flavor: extraction, isolation and quantification of vanillin and others constituents, Int. J. Food Sci. Nutr. 59 (4) (2008) 299–326.
[8] S.S. Arya, et al., Vanillin: A review on the therapeutic prospects of a popular flavouring molecule, Adv. Tradit. Med. 21 (3) (2021) 1–17.
[9] D.P. Bezerra, A.K.N. Soares, D.P. de Sousa, Overview of the role of vanillin on redox status and cancer development, Oxid. Med. Cell. Longev. 2016 (1) (2016) 9734816.
[10] C.S. Bezerra-Filho, et al., Therapeutic potential of vanillin and its main metabolites to regulate the inflammatory response and oxidative stress, Mini Rev. Med. Chem. 19 (20) (2019) 1681–1693.
[11] A. Tai, et al., Evaluation of antioxidant activity of vanillin by using multiple antioxidant assays, Biochim. Et. Biophys. Acta (BBA)-General. Subj. 1810 (2) (2011) 170–177.
[12] F. Joint, W.E.Co.F. Additives, Safety evaluation of certain food additives and contaminants, World Health Organization, 2002.
[13] E.Po Additives, and P.o.S.u.i.A. Feed, *Scientific Opinion on the safety and efficacy of benzyl alcohols, aldehydes, acids, esters and acetals (chemical group 23) when used as flavourings for all animal species*, EFSA J. 10 (7) (2012) 2785.
[14] K. Gokulkumar, et al., Nanoparticles of SnS on carbon nanofibers for electrochemical detection of vanillin, ACS Appl. Nano Mater. 7 (11) (2024) 13183–13193.
[15] K. Gokulkumar, et al., Engineered ZnS: SnS2/Bi2S3 hierarchically porous heterostructure with accelerated charge transfer for trace level electrochemical detection of azathioprine, J. Environ. Chem. Eng. (2026) 123587.
[16] K. Gokulkumar, et al., Plasma-activated O-Nd2WO6/f-CNF hybrid electrode for sensitive electrochemical detection of azathioprine in environmental water samples, J. Environ. Chem. Eng. (2026) 123120.
[17] P. Varatharajan, et al., Structural Engineering of Hierarchical NiFe-LDH/MXene Composites on SPCE for Ultrasensitive Electrochemical Detection of Metol, Surf. Interfaces (2025) 108273.
[18] M.W. Dong, Modern HPLC for practicing scientists, John Wiley & Sons, 2006.
[19] C. Hao, X. Zhao, P. Yang, GC-MS and HPLC-MS analysis of bioactive pharmaceuticals and personal-care products in environmental matrices, TrAC. Trends Anal. Chem. 26 (6) (2007) 569–580.
[20] D. Steiner, et al., Challenges and future directions in LC-MS-based multiclass method development for the quantification of food contaminants, Anal. Bioanal. Chem. 413 (1) (2021) 25–34.

[21] P. Manimaran, et al., Ni-Metal–Organic Framework/β-Cyclodextrin/Functionalized Carbon Black Nanomaterials for Enhanced Electrochemical Sensing of Metronidazole in Environmental and Clinical Samples, ACS Appl. Nano Mater. 8 (48) (2025) 23260–23272.
[22] H. Furukawa, et al., The chemistry and applications of metal-organic frameworks, Science 341 (6149) (2013) 1230444.
[23] R.-B. Lin, Z. Zhang, B. Chen, Achieving high performance metal–organic framework materials through pore engineering, Acc. Chem. Res. 54 (17) (2021) 3362–3376.
[24] H. Zhang, et al., Metal-organic-framework-based materials as platforms for renewable energy and environmental applications, Joule 1 (1) (2017) 77–107.
[25] W. Xia, et al., Metal–organic frameworks and their derived nanostructures for electrochemical energy storage and conversion, Energy & Environ. Sci. 8 (7) (2015) 1837–1866.
[26] R.R. Salunkhe, Y.V. Kaneti, Y. Yamauchi, Metal–organic framework-derived nanoporous metal oxides toward supercapacitor applications: progress and prospects, ACS nano 11 (6) (2017) 5293–5308.
[27] P. Varatharajan, et al., Advancement and growth of metal organic framework derived nanostructured materials for fabrication of high energy density supercapacitors, J. Power Sources 687 (2026) 240526.
[28] T. Qiu, et al., Pristine hollow metal–organic frameworks: design, synthesis and application, Angew. Chem. Int. Ed. 60 (32) (2021) 17314–17336.
[29] H. Wang, Q. Gao, L. Jiang, Facile approach to prepare nickel cobaltite nanowire materials for supercapacitors, Small (Weinh. der Bergstr. Ger.) 7 (17) (2011) 2454–2459.
[30] Z.H. Shah, et al., Highly enhanced plasmonic photocatalytic activity of Ag/AgCl/TiO 2 by CuO co-catalyst, J. Mater. Chem. A 3 (7) (2015) 3568–3575.
[31] W. Lu, et al., State of the art of carbon nanotube fibers: opportunities and challenges, Adv. Mater. 24 (14) (2012) 1805–1833.
[32] Q. Li, et al., Structure-dependent electrical properties of carbon nanotube fibers, Adv. Mater. 19 (20) (2007) 3358–3363.
[33] J. Wang, et al., MOF-derived hollow multi-shell NiCo 2 O 4 spheres as high-performance cathodes for alkaline aqueous Zn batteries, New. J. Chem. 50 (21) (2026) 9111–9119.
[34] Chavi Mahala, Mrinmoyee Basu, Nanosheets of NiCo2O4/NiO as Efficient and Stable Electrocatalyst for Oxygen Evolution Reaction, ACS Omega 2 (11) (2017) 7559–7567, https://doi.org/10.1021/acsomega.7b00957. https://pubs.acs.org/acsodf/article/2/11/7559/751201/Nanosheets-of-NiCo2O4-NiO-as-Efficient-and-Stable. (Accessed 2 November 2017).
[35] M. Eskandari, et al., NiCo2O4-based nanostructured composites for high-performance pseudocapacitor electrodes, Colloids Surf. A Physicochem. Eng. Asp. 584 (2020) 124039.
[36] X. Xiao, et al., Macro-/meso-porous NiCo2O4 synthesized by template-free solution combustion to enhance the performance of a nonenzymatic amperometric glucose sensor, Microchim. Acta 187 (1) (2020) 64.
[37] P. Varatharajan, et al., Ultrasonic synthesis of MOF-based hybrid composite for electrochemical detection of furazolidone antibiotic in food and biological samples, Surf. Interfaces 55 (2024) 105384.
[38] K. Gokulkumar, I.J.D. Priscillal, S.-F. Wang, Deep eutectic solvent-mediated synthesis of PDA coated f-CNF doped ZnS nanoparticles for electrode modification: Innovative sensing platform for determination of pollutant 3-nitrophenol, J. Alloy. Compd. 924 (2022) 166561.
[39] M.-C. Liu, et al., A sol–gel process for fabrication of NiO/NiCo2O4/Co3O4 composite with improved electrochemical behavior for electrochemical capacitors, ACS Appl. Mater. & Interfaces 4 (9) (2012) 4631–4636.
[40] S. Subramani, G. Rajamanickam, V. Panneerselvam, Urchin-like Hierarchical Cu-NiCo2O4/g-C3N4 Nanostructures as Advanced Electrode Materials for High-Performance Supercapacitors, ACS Appl. Eng. Mater. 4 (4) (2026) 1638–1651.
[41] S.-J. Huang, et al., Synthesis and characterization of Bi2S3-embedded carbon nanofibers as a novel electrochemical biosensor for the detection of mycotoxin zearalenone in food crops, FlatChem 45 (2024) 100652.
[42] S.-J. Huang, et al., Nanoarchitectonics of europium vanadate nanoparticles decorated carbon nanofibers for electrochemical detection of fungicide in fruits, J. Taiwan. Inst. Chem. Eng. 161 (2024) 105563.
[43] E. Laviron, General expression of the linear potential sweep voltammogram in the case of diffusionless electrochemical systems, J. Electroanal. Chem. Interfacial Electrochem. 101 (1) (1979) 19–28.
[44] N. Nardi, et al., Titanium carbide MXene-supported gold nanoparticles and exfoliated graphite nanoplatelets: A multifunctional platform for electrochemical sensing, FlatChem (2026) 100997.
[45] I. Kouhi, et al., Development of an electrochemical sensor for determination of vanillin in some food stuffs, J. Food Process. Preserv. 46 (2) (2022) e16289.
[46] V.S. Manikandan, et al., Electrochemical sensing of vanillin based on fluorine-doped reduced graphene oxide decorated with gold nanoparticles, Foods 11 (10) (2022) 1448.
[47] K. Periyasamy, et al., Electrochemical monitoring of vanillin using BaFe12O18@ carbon black modified electrode in food samples, Food Chem. (2025) 147306.
[48] S. Dehdashtian, et al., Determination of vanillin in different food samples by using SMM/Au@ ZIF-67 electrochemical sensor, Sci. Rep. 13 (1) (2023) 17907.
[49] D.D. Khandagale, S.-F. Wang, Urchin-like Bi2S3 modified disposable SPCE for vanillin detection: Experimental and DFT insights into the oxidation mechanism, Food Chem. (2026) 148757.
[50] L. Taouri, et al., Fullerene-MWCNT nanostructured-based electrochemical sensor for the detection of Vanillin as food additive, J. Food Compos. Anal. 100 (2021) 103811.
[51] A. Ramzannezhad, et al., Development of electrochemical sensor for vanillin determination using carbon spheres–LaFe0. 9Ni0. 1O3 nanohybrid, Sci. Rep. 15 (1) (2025) 37624.
[52] A. Govindharaj, et al., An electrochemical signal amplification using functionalized carbon nanofiber integrated manganese molybdate nanocomposite for rapid detection of vanillin in food samples, Food Chem. 475 (2025) 143334.
[53] P. Deng, X. Nie, W. Peng, Quantification of vanillin based on a high-performance electrochemical sensor utilizing Ni3S4/Co3S4-ErGO composite, Microchem. J. (2025) 114837.
[54] A. Ramzannezhad, S. Ghasemi, S. Safari, Manganese-nickel cobaltite/graphitic carbon nitride/cerium oxide nanocomposite for vanillin sensing in food samples, Sci. Rep. (2026).
[55] S.A. Hira, J. Quintal, A. Chen, Sensitive electrochemical determination of vanillin using a bimetallic hydroxide and reduced graphene oxide nanocomposite, Sensors 25 (6) (2025) 1694.
[56] R. Zaimbashi, T. Shamspur, A. Mostafavi, An electrochemical sensing platform based on zirconium UiO 66 metal-organic framework for determination of vanillin in the presence of folic acid, Sci. Rep. (2026).